

## Non-hydrostatic modeling of wave interactions with porous structures



Gangfeng Ma <sup>a,\*</sup>, Fengyan Shi <sup>b</sup>, Shih-Chun Hsiao <sup>c</sup>, Yun-Ta Wu <sup>c</sup>

<sup>a</sup> Department of Civil and Environmental Engineering, Old Dominion University, Norfolk, VA, USA

<sup>b</sup> Center for Applied Coastal Research, University of Delaware, Newark, DE, USA

<sup>c</sup> Department of Hydraulic and Ocean Engineering, National Cheng Kung University, Tainan, Taiwan

### ARTICLE INFO

#### Article history:

Received 19 March 2014

Received in revised form 14 May 2014

Accepted 19 May 2014

Available online 11 June 2014

#### Keywords:

Wave–structure interactions

Non-hydrostatic model

Porous media

NHWAVE

### ABSTRACT

This paper presents a three-dimensional non-hydrostatic wave model NHWAVE for simulating wave interactions with porous structures. The model calculates the porous media flow based on well-balanced volume-averaged Reynolds-averaged Navier–Stokes equations (VARANS) in  $\sigma$  coordinate. The turbulence field within the porous structures is simulated by an improved  $k - \epsilon$  model. To account for the temporally varying porosity at the grid cell center introduced by the variation of free surface elevation, the porosity is updated at each time step in the computation. The model is calibrated and validated using a wide range of laboratory measurements, involving dam-break flow through porous media, 3D solitary wave interactions with a porous structure, 2D solitary wave interactions with a submerged permeable obstacle as well as periodic wave breaking over a submerged porous breakwater with steep slopes. The model is shown to be capable of well simulating wave reflection, diffraction, wave breaking and wave transmission through porous structures, as well as the turbulent flow field around the permeable structures. It is also demonstrated in the paper that the current non-hydrostatic model is computationally much more efficient than the existing porous flow models based on VOF approach. The non-hydrostatic wave model NHWAVE can be a useful tool for studying wave–structure interactions.

Published by Elsevier B.V.

### 1. Introduction

Porous structures are widely used in coastal engineering to reduce wave impact and protect shoreline as well as impervious breakwaters. For example, porous armor layers built of concrete pieces or crushed rocks are frequently used to protect rubble mound breakwaters. Accurate calculation of porous media flow as well as pressure and force distributions in porous structures is needed for the design of breakwaters.

A great number of numerical models have been developed to simulate the wave action on and within porous structures in the last few decades. The first attempt was conducted by van Gent (1994), who coupled a one-dimensional shallow-water equation model with a porous flow model to predict flow properties and forces on permeable structures under wave actions. After then, models that were based on mild-slope equations (Hsu et al., 2008; Losada et al., 1996) and Boussinesq equations (Chen, 2006; Cruz et al., 1997; Hsiao et al., 2002, 2010) were developed to study wave reflection, transmission and diffraction on the porous structures. Recent numerical studies were focused on solving volume-averaged Reynolds-averaged Navier–Stokes equations (VARANS) with free surface, which was captured by the volume-of-fluid (VOF) approach. For example, Liu et al. (1999) presented a 2D VOF model for simulating wave interaction with porous structures. Their model was based on the

assumption that the turbulence within the porous media is negligible. Hsu et al. (2002) extended the model to include a  $k - \epsilon$  turbulence closure within the porous structures, making it applicable for turbulent porous flow. del Jesus et al. (2012) extended the VARANS equations to the most general scenario taking into account the spatial variation of porosity. Using these three approaches, a series of VOF models have been developed for studying wave interactions with porous structures, for instance, COBRAS (Hsu et al., 2002; Liu et al., 1999; Wu and Hsiao, 2013), IH-2VOF (Lara et al., 2006), IH-3VOF (del Jesus et al., 2012; Lara et al., 2012), OpenFOAM (Higuera et al., 2014a,b) and Truchas (Hu et al., 2012; Wu et al., 2014).

Although VOF models have been proven to be capable of simulating wave–structure interactions, they are well-known for computational inefficiency. An alternative to the VOF model is the non-hydrostatic wave model, which has shown great potential for resolving wave dynamics in the surf zone, including wave breaking (Ma et al., 2012; Smit et al., 2013; Zijlema and Stelling, 2008), nonlinear wave dynamics (Smit et al., 2014) as well as infragravity wave motions (Ma et al., 2014a; Rijnsdorp et al., 2014). Comparing to the VOF models, the non-hydrostatic wave models assume that the free surface is a single value function of horizontal coordinates. Thus the Navier–Stokes equations are greatly simplified, resulting in an explicit equation for free surface elevation. This simplification would lead to much more efficient computation of free surface elevation, although it results in two major drawbacks. One is that the free surface must be continuous. The model is not able to simulate the flow that the free surface is disconnected by

\* Corresponding author. Tel.: +1 757 683 4732.

E-mail address: [gma@odu.edu](mailto:gma@odu.edu) (G. Ma).

impervious structures. The other is that the model cannot capture complicated free surface, for instance, in plunging breaking waves.

In this paper, we present a non-hydrostatic wave-resolving model for simulating wave interactions with porous structures. The model is based on NHWAVE, which was originally developed by Ma et al. (2012). NHWAVE has been applied to study wave–vegetation interactions (Ma et al., 2013a), tsunami waves generated by submarine landslide (Ma et al., 2013b) and rip currents in the field-scale surf zone (Ma et al., 2014b). It was shown to be capable of simulating wave dynamics in both the laboratory and field-scale problems.

The remainder of the paper is organized as follows. The model equations for the porous media flow are derived in Section 2. The turbulence closure taking into account the spatial variation of porosity is introduced in Section 3. The numerical schemes and boundary conditions are presented in Section 4. The model is then utilized to reproduce measurements in four laboratory experiments, involving dam-break flow through porous media, 3D solitary wave interactions with a vertical porous breakwater, 2D solitary wave interaction with a submerged permeable obstacle and periodic wave breaking over a submerged porous breakwater with steep slopes. The results are presented and discussed in Section 5. The conclusions are made in Section 6.

## 2. Model equations

The volume-averaged Reynolds-averaged Navier–Stokes equations (VARANS) (del Jesus et al., 2012; Hsu et al., 2002) governing the flow motion in the porous structures are derived using the macroscopic approach, which describes a mean behavior of the flow field by averaging its properties over control volumes (Higuera et al., 2014). The current model solves the VARANS formulation given by del Jesus et al. (2012), which reads

$$\frac{\partial}{\partial x_i^*} \frac{u_i}{n} = 0 \quad (1)$$

$$\frac{\partial}{\partial t^*} \frac{u_i}{n} + \frac{u_j}{n} \frac{\partial}{\partial x_j^*} \frac{u_i}{n} = -\frac{1}{\rho} \frac{\partial p}{\partial x_i^*} + g_i + \frac{\partial}{\partial x_j^*} \left[ (\nu + \nu_t) \frac{\partial}{\partial x_i^*} \frac{u_i}{n} \right] + R \frac{u_i}{n} \quad (2)$$

in which  $(i,j) = 1,2,3$ ,  $x_i^*$  is Cartesian coordinate,  $u_i$  is velocity component in the  $x_i^*$  direction,  $n$  is porosity,  $p$  is total pressure,  $\rho$  is water density,  $g_i = -g\delta_{i3}$  is gravitational body force, and  $\nu$  and  $\nu_t$  are laminar and turbulent kinematic viscosities, respectively. The last term in Eq. (2) accounts for frictional forces, pressure forces and added mass in the porous media, which is given by

$$R = -a_p - b_p \left| \frac{\mathbf{u}}{n} \right| - c_p \frac{\partial}{\partial t} \quad (3)$$

where the first term represents the frictional force induced by viscous effect, the second term accounts for the turbulence effect and the last term models the added mass effect for accelerating fluid in the porous media.  $|\mathbf{u}|$  is the magnitude of the flow velocity  $|\mathbf{u}| = \sqrt{\sum_i u_i^2}$ . The three parameters are given by van Gent (1994) and Liu et al. (1999)

$$a_p = \alpha \frac{(1-n)^2}{n^2} \frac{\nu}{D_{50}^2} \quad (4)$$

$$b_p = \beta \left( 1 + \frac{7.5}{KC} \right) \frac{1-n}{n^2} \frac{1}{D_{50}} \quad (5)$$

$$c_p = \gamma \frac{1-n}{n} \quad (6)$$

in which  $\alpha$  and  $\beta$  are coefficients to be determined.  $\gamma$  is an empirical coefficient that is usually taken as 0.34 (Liu et al., 1999).  $D_{50}$  is the characteristic diameter of the porous materials.  $KC$  is the Keulegan–Carpenter number representing the ratio of the characteristic length scale of fluid particle motion to that of porous media, defined as  $KC = |\mathbf{u}|T/(nD_{50})$ , where  $T$  is the typical wave period.

To capture the free surface, a  $\sigma$ -coordinate is introduced.

$$t = t^* \quad x = x^* \quad y = y^* \quad \sigma = \frac{z^* + h}{D} \quad (7)$$

where  $D(x,y,t) = h(x,y) + \eta(x,y,t)$ ,  $h$  is water depth, and  $\eta$  is surface elevation. This coordinate transformation maps the varying vertical coordinate in the physical domain to a transformed space where  $\sigma$  spans from 0 to 1. In the  $\sigma$  coordinate system, Eqs. (1) and (2) written in a well-balanced form are given by

$$\frac{\partial D}{\partial t} + \frac{\partial}{\partial x} \frac{n}{n} + \frac{\partial}{\partial y} \frac{n}{n} + \frac{\partial}{\partial \sigma} \frac{\omega}{n} = 0 \quad (8)$$

$$(1 + c_p) \frac{\partial \mathbf{U}}{\partial t} + \frac{\partial \mathbf{F}}{\partial x} + \frac{\partial \mathbf{G}}{\partial y} + \frac{\partial \mathbf{H}}{\partial \sigma} = \mathbf{S}_h + \mathbf{S}_p + \mathbf{S}_\tau + \mathbf{S}_r \quad (9)$$

where  $\mathbf{U} = (\frac{Du}{n}, \frac{Dv}{n}, \frac{Dw}{n})^T$ . The well-balanced fluxes are given by

$$\mathbf{F} = \begin{pmatrix} \frac{Duu}{n^2} + \frac{1}{2} g \eta^2 + g h \eta \\ \frac{Duv}{n^2} \\ \frac{Duw}{n^2} \end{pmatrix} \quad \mathbf{G} = \begin{pmatrix} \frac{Duv}{n^2} \\ \frac{Dvv}{n^2} + \frac{1}{2} g \eta^2 + g h \eta \\ \frac{Dvw}{n^2} \end{pmatrix} \quad \mathbf{H} = \begin{pmatrix} \frac{u \omega}{n^2} \\ \frac{v \omega}{n^2} \\ \frac{w \omega}{n^2} \end{pmatrix}$$

and the first three source terms are formulated as

$$\mathbf{S}_h = \begin{pmatrix} g D \frac{\partial h}{\partial x} \\ g D \frac{\partial h}{\partial y} \\ 0 \end{pmatrix} \quad \mathbf{S}_p = \begin{pmatrix} -\frac{D}{\rho} \left( \frac{\partial p}{\partial x} + \frac{\partial p}{\partial \sigma} \frac{\partial \sigma}{\partial x^*} \right) \\ -\frac{D}{\rho} \left( \frac{\partial p}{\partial y} + \frac{\partial p}{\partial \sigma} \frac{\partial \sigma}{\partial y^*} \right) \\ -\frac{1}{\rho} \frac{\partial p}{\partial \sigma} \end{pmatrix} \quad \mathbf{S}_\tau = \begin{pmatrix} DS_{\tau_x} \\ DS_{\tau_y} \\ DS_{\tau_z} \end{pmatrix}.$$

The fourth source term is written as

$$\mathbf{S}_r = \begin{pmatrix} -a_p \frac{Du}{n} - b_p \left| \frac{\mathbf{u}}{n} \right| \frac{Du}{n} + c_p \frac{u \partial D}{n \partial t} \\ -a_p \frac{Dv}{n} - b_p \left| \frac{\mathbf{u}}{n} \right| \frac{Dv}{n} + c_p \frac{v \partial D}{n \partial t} \\ -a_p \frac{Dw}{n} - b_p \left| \frac{\mathbf{u}}{n} \right| \frac{Dw}{n} + c_p \frac{w \partial D}{n \partial t} \end{pmatrix}.$$

It should be pointed out that, in the  $\sigma$ -coordinate models, the porosity at the grid cell center is temporally and spatially varying along with the variation of free surface elevation. Therefore, the porosity  $n$  must be included inside the derivatives. Moreover, the porosity has to be updated at each time step in the computation. This is different from the z-coordinate models such as the existing VOF models, in which the porosity is not temporally varying so that it can be prescribed without need to be updated in the computation.

In these source terms, the total pressure has been separated into two parts: dynamic pressure  $p$  (use  $p$  as dynamic pressure hereinafter for simplicity) and hydrostatic pressure  $\rho g(\eta - z)$ .  $DS_{\tau_x}$ ,  $DS_{\tau_y}$ , and  $DS_{\tau_z}$

are turbulent diffusion terms. The vertical velocity  $\omega$  in  $\sigma$  coordinate is expressed as

$$\frac{\omega}{n} = D \left( \frac{\partial \sigma}{\partial t^*} + \frac{u}{n} \frac{\partial \sigma}{\partial x^*} + \frac{v}{n} \frac{\partial \sigma}{\partial y^*} + \frac{w}{n} \frac{\partial \sigma}{\partial z^*} \right) \quad (10)$$

with

$$\begin{aligned} \frac{\partial \sigma}{\partial t^*} &= -\frac{\sigma \partial D}{D \partial t} \\ \frac{\partial \sigma}{\partial x^*} &= \frac{1}{D} \frac{\partial h}{\partial x} - \frac{\sigma \partial D}{D \partial x} \\ \frac{\partial \sigma}{\partial y^*} &= \frac{1}{D} \frac{\partial h}{\partial y} - \frac{\sigma \partial D}{D \partial y} \\ \frac{\partial \sigma}{\partial z^*} &= \frac{1}{D}. \end{aligned} \quad (11)$$

Clearly, if the porosity  $n$  equals unity, the governing equations return to the Reynolds-averaged Navier-Stokes equations in original NHWAVE (Ma et al., 2012).

To solve water depth  $D$ , we integrate the continuity Eq. (8) from  $\sigma = 0$  to 1 and use the boundary conditions at the surface and bottom for  $\omega$ .

$$\frac{\partial D}{\partial t} + \frac{\partial}{\partial x} \left( D \int_0^1 \frac{u}{n} d\sigma \right) + \frac{\partial}{\partial y} \left( D \int_0^1 \frac{v}{n} d\sigma \right) = 0 \quad (12)$$

### 3. Turbulence closure

The volume-averaging approach can also be applied to the  $k - \epsilon$  equations. The Darcy's volume-averaged eddy viscosity is calculated as (Hsu et al., 2002)

$$\nu_t = C_\mu \frac{k^2}{n}. \quad (13)$$

The volume-averaged  $k - \epsilon$  equations (del Jesus et al., 2012) written in conservative forms are

$$\frac{\partial}{\partial t} \left( \frac{Dk}{n} \right) + \nabla \cdot \left( \frac{D\mathbf{u}k}{n^2} \right) = \nabla \cdot \left[ D \left( \nu + \frac{\nu_t}{\sigma_k} \right) \nabla \frac{k}{n} \right] + D(P_s - \frac{\epsilon}{n}) + D\epsilon_\infty \quad (14)$$

$$\begin{aligned} \frac{\partial}{\partial t} \left( \frac{D\epsilon}{n} \right) + \nabla \cdot \left( \frac{D\mathbf{u}\epsilon}{n^2} \right) &= \nabla \cdot \left[ D \left( \nu + \frac{\nu_t}{\sigma_\epsilon} \right) \nabla \frac{\epsilon}{n} \right] + \frac{\epsilon}{k} D \left( C_{1\epsilon} P_s - C_{2\epsilon} \frac{\epsilon}{n} \right) \\ &+ D C_{2\epsilon} \frac{\epsilon_\infty}{k_\infty} \end{aligned} \quad (15)$$

where  $k$  and  $\epsilon$  are the Darcy's volume-averaged turbulent kinetic energy and turbulent dissipation rate, respectively.  $\epsilon_\infty$  and  $k_\infty$  are closures for porous media flow, which are given by Hsu et al. (2002) and Nakayama and Kuwahara (1999):

$$\epsilon_\infty = 39.0 \frac{(1-n)^{2.5}}{n} \left( \sum_i u_i^2 \right)^{3/2} \frac{1}{D_{50}} \quad (16)$$

$$k_\infty = 3.7 \frac{(1-n)}{\sqrt{n}} \sum_i u_i^2 \quad (17)$$

where  $\sigma_k, \sigma_\epsilon, C_{1\epsilon}, C_{2\epsilon}$ , and  $C_\mu$  are empirical coefficients (Rodi, 1987).

$$\sigma_k = 1.0, \quad \sigma_\epsilon = 1.3, \quad C_{1\epsilon} = 1.44, \quad C_{2\epsilon} = 1.92, \quad C_\mu = 0.09 \quad (18)$$

$P_s$  is the shear production, which is computed as

$$P_s = -\overline{u'_i u'_j} \frac{\partial u_i^*}{\partial x_j^*} \quad (19)$$

where the Reynolds stress  $\overline{u'_i u'_j}$  is calculated by a nonlinear model proposed by Lin and Liu (1998) and modified by Hsu et al. (2002) for porous media flow. We further modify it to include the porosity inside the derivatives, resulting in the following form.

$$\begin{aligned} \overline{u'_i u'_j} &= -C_d \frac{k^2}{n\epsilon} \left( \frac{\partial u_i^*}{\partial x_j^*} + \frac{\partial u_j^*}{\partial x_i^*} \right) + \frac{2k}{3n} \delta_{ij} \\ &- C_1 \frac{k^3}{n\epsilon^2} \left( \frac{\partial u_i^*}{\partial x_l^*} \frac{\partial u_l^*}{\partial x_j^*} + \frac{\partial u_j^*}{\partial x_l^*} \frac{\partial u_l^*}{\partial x_i^*} - \frac{2}{3} \frac{\partial u_l^*}{\partial x_k^*} \frac{\partial u_k^*}{\partial x_i^*} \delta_{ij} \right) \\ &- C_2 \frac{k^3}{n\epsilon^2} \left( \frac{\partial u_i^*}{\partial x_k^*} \frac{\partial u_k^*}{\partial x_j^*} - \frac{1}{3} \frac{\partial u_l^*}{\partial x_k^*} \frac{\partial u_l^*}{\partial x_k^*} \delta_{ij} \right) \\ &- C_3 \frac{k^3}{n\epsilon^2} \left( \frac{\partial u_k^*}{\partial x_i^*} \frac{\partial u_k^*}{\partial x_j^*} - \frac{1}{3} \frac{\partial u_l^*}{\partial x_k^*} \frac{\partial u_l^*}{\partial x_k^*} \delta_{ij} \right) \end{aligned} \quad (20)$$

in which the flow velocity  $u_i^* = u_i/n$ .  $C_d, C_1, C_2$  and  $C_3$  are empirical coefficients given by Lin and Liu (1998).

$$\begin{aligned} C_d &= \frac{2}{3} \left( \frac{1}{7.4 + 2S_{max}} \right), \quad C_1 = \frac{1}{185.2 + 3D_{max}^2} \\ C_2 &= -\frac{1}{58.5 + 2D_{max}^2}, \quad C_3 = \frac{1}{370.4 + 3D_{max}^2} \end{aligned} \quad (21)$$

with

$$\begin{aligned} S_{max} &= \frac{k}{\epsilon} \max \left\{ \left| \frac{\partial u_i^*}{\partial x_i^*} \right| \text{(indices not summed)} \right\} \\ D_{max} &= \frac{k}{\epsilon} \max \left\{ \left| \frac{\partial u_i^*}{\partial x_j^*} \right| \right\}. \end{aligned} \quad (22)$$

### 4. Numerical schemes and boundary conditions

Following the framework of NHWAVE (Ma et al., 2012), we solve the model equations using a combined finite volume/finite difference method. A shock-capturing HLL TVD scheme is used to discretize the momentum equations and estimate fluxes at cell faces. For  $k - \epsilon$  equations, the convective fluxes are determined by the hybrid linear/parabolic approximation (HLPA) scheme (Zhu, 1991), which has second-order accuracy in space. The two-stage second-order nonlinear Strong Stability-Preserving (SSP) Runge-Kutta scheme (Gottlieb et al., 2001) is adopted for time stepping in order to obtain second-order temporal accuracy. At the first stage, an intermediate quantity  $\mathbf{U}^{(1)}$  is evaluated using a typical first-order, two-step projection method given by

$$(1 + c_p) \frac{\mathbf{U}^* - \mathbf{U}^n}{\Delta t} = - \left( \frac{\partial \mathbf{F}}{\partial x} + \frac{\partial \mathbf{G}}{\partial y} + \frac{\partial \mathbf{H}}{\partial z} \right)^n + \mathbf{S}_h^n + \mathbf{S}_r^n + \mathbf{S}_r^{(1)} \quad (23)$$

$$(1 + c_p) \frac{\mathbf{U}^{(1)} - \mathbf{U}^*}{\Delta t} = \mathbf{S}_p^{(1)} \quad (24)$$

where  $\mathbf{U}^n$  represents  $\mathbf{U}$  value at time level  $n$ ,  $\mathbf{U}^*$  is the intermediate value in the two-step projection method, and  $\mathbf{U}^{(1)}$  is the final first stage estimate. Notice that the source term associated with porous media is evaluated implicitly.

At the second stage, the velocity field is updated to a second intermediate level using the same projection method, after which the

Runge–Kutta algorithm is used to obtain a final value of the solution at the  $n + 1$  time level.

$$(1 + c_p) \frac{\mathbf{U}^* - \mathbf{U}^{(1)}}{\Delta t} = -\left(\frac{\partial \mathbf{F}}{\partial x} + \frac{\partial \mathbf{G}}{\partial y} + \frac{\partial \mathbf{H}}{\partial \sigma}\right)^{(1)} + \mathbf{S}_h^{(1)} + \mathbf{S}_r^{(1)} + \mathbf{S}_r^{(2)} \quad (25)$$

$$(1 + c_p) \frac{\mathbf{U}^{(2)} - \mathbf{U}^*}{\Delta t} = \mathbf{S}_p^{(2)} \quad (26)$$

$$\mathbf{U}^{n+1} = \frac{1}{2} \mathbf{U}^n + \frac{1}{2} \mathbf{U}^{(2)}. \quad (27)$$

At each stage, the surface elevation is obtained by solving Eq. (12) explicitly. The time step  $\Delta t$  is adaptive during the simulation, following the Courant–Friedrichs–Lowy (CFL) criterion, which is taken as 0.5 to ensure numerical stability. Each stage of the calculation requires the specification of the nonhydrostatic component of the pressure force as expressed through the quantities  $\mathbf{S}_p$ . The dynamic pressure field is obtained by solving the Poisson equation. From Eqs. (24) or (26), we get

$$(1 + c_p) \left(\frac{u}{n}\right)^{(k)} = (1 + c_p) \left(\frac{u}{n}\right)^* - \frac{\Delta t}{\rho} \left(\frac{\partial p}{\partial x} + \frac{\partial p}{\partial \sigma} \frac{\partial \sigma}{\partial x^*}\right)^{(k)} \quad (28)$$

$$(1 + c_p) \left(\frac{v}{n}\right)^{(k)} = (1 + c_p) \left(\frac{v}{n}\right)^* - \frac{\Delta t}{\rho} \left(\frac{\partial p}{\partial y} + \frac{\partial p}{\partial \sigma} \frac{\partial \sigma}{\partial y^*}\right)^{(k)} \quad (29)$$

$$(1 + c_p) \left(\frac{w}{n}\right)^{(k)} = (1 + c_p) \left(\frac{w}{n}\right)^* - \frac{\Delta t}{\rho} \frac{1}{D^{(k)}} \frac{\partial p}{\partial \sigma} \quad (30)$$

where  $k = 1, 2$  represents the  $k$ th stage in the Runge–Kutta integration.

In the  $\sigma$ -coordinate system, the continuity in Eq. (1) is rewritten as

$$\frac{\partial u}{\partial x} n + \frac{\partial}{\partial \sigma} \left(\frac{u}{n}\right) \frac{\partial \sigma}{\partial x^*} + \frac{\partial v}{\partial y} n + \frac{\partial}{\partial \sigma} \left(\frac{v}{n}\right) \frac{\partial \sigma}{\partial y^*} + \frac{1}{D} \frac{\partial w}{\partial \sigma} n = 0. \quad (31)$$

Substituting Eqs. (28)–(30) into Eq. (31), we obtain the Poisson equation in  $(x, y, \sigma)$  coordinate system

$$\begin{aligned} & \frac{\partial}{\partial x} \left[ \frac{\partial p}{\partial x} + \frac{\partial p}{\partial \sigma} \frac{\partial \sigma}{\partial x^*} \right] + \frac{\partial}{\partial y} \left[ \frac{\partial p}{\partial y} + \frac{\partial p}{\partial \sigma} \frac{\partial \sigma}{\partial y^*} \right] + \frac{\partial}{\partial \sigma} \left( \frac{\partial p}{\partial x} \right) \frac{\partial \sigma}{\partial x^*} \\ & + \frac{\partial}{\partial \sigma} \left( \frac{\partial p}{\partial y} \right) \frac{\partial \sigma}{\partial y^*} + \left[ \left( \frac{\partial \sigma}{\partial x^*} \right)^2 + \left( \frac{\partial \sigma}{\partial y^*} \right)^2 + \frac{1}{D^2} \right] \frac{\partial}{\partial \sigma} \left( \frac{\partial p}{\partial \sigma} \right) \\ & = (1 + c_p) \frac{\rho}{\Delta t} \left( \frac{\partial}{\partial x} \left(\frac{u}{n}\right)^* + \frac{\partial}{\partial \sigma} \left(\frac{u}{n}\right)^* \frac{\partial \sigma}{\partial x^*} + \frac{\partial}{\partial y} \left(\frac{v}{n}\right)^* \right. \\ & \left. + \frac{\partial}{\partial \sigma} \left(\frac{v}{n}\right)^* \frac{\partial \sigma}{\partial y^*} + \frac{1}{D} \frac{\partial}{\partial \sigma} \left(\frac{w}{n}\right)^* \right). \end{aligned} \quad (32)$$

The above equation is discretized with the second-order space-centered finite difference method, resulting in an asymmetric coefficient matrix with a total of 15 diagonal lines. The linear system is solved using the high performance preconditioner HYPRE software library. The model is fully parallelized using Message Passing Interface (MPI) with non-blocking communication.

To solve the equations, boundary conditions are required for all the physical boundaries. Specifically, at the free surface, we have

$$\frac{\partial u}{\partial \sigma}|_{\sigma=1} = \frac{\partial v}{\partial \sigma}|_{\sigma=1} = 0, \quad \frac{w}{n}|_{\sigma=1} = \frac{\partial \eta}{\partial t} + \frac{u}{n} \frac{\partial \eta}{\partial x} + \frac{v}{n} \frac{\partial \eta}{\partial y}. \quad (33)$$

Dynamic pressure is zero at the free surface. For the  $k - \epsilon$  model, zero gradients of  $k$  and  $\epsilon$  are imposed.

$$\frac{\partial k}{\partial \sigma}|_{\sigma=1} = \frac{\partial \epsilon}{\partial \sigma}|_{\sigma=1} = 0 \quad (34)$$

At the bottom, the normal velocity and the tangential stress are prescribed. The normal velocity  $w$  is imposed through the kinematic boundary condition.

$$\frac{w}{n}|_{\sigma=0} = -\frac{u}{n} \frac{\partial h}{\partial x} - \frac{v}{n} \frac{\partial h}{\partial y} \quad (35)$$

## 5. Results and discussions

In this section, the non-hydrostatic wave model NHWAVE with the new implementation is validated against laboratory measurements. Firstly, the model is used to reproduce the two-dimensional dam break flow through porous media (Liu et al., 1999). Secondly, the model is validated against laboratory measurements of 3D solitary wave interaction with a vertical porous obstacle, as presented in Lara et al. (2012). Thirdly, the model is employed to simulate flow and turbulence field around a submerged porous structure under a solitary wave (Wu and Hsiao, 2013). Finally, the model is tested against the laboratory measurements for wave breaking over a submerged porous breakwater with steep slopes (Hieu and Tanimoto, 2006).

### 5.1. Two-dimensional porous dam-break

The model is firstly validated against the laboratory measurements of dam-break flow through porous media conducted by Liu et al. (1999). The experiments were performed in a wave tank that is 89.2 cm long, 44 cm wide and 58 cm high. The porous dam that is 29 cm long, 44 cm wide and 37 cm high was located at the center of the tank with  $x = 30.0$ –59.0 cm. We conducted 2D simulations with the domain length of 89.2 cm, discretized by 178 horizontal cells. The porous materials were crushed rocks with a grain size of 1.59 cm and a porosity of 0.49. In this case, the flow through the porous dam is fully turbulent. Therefore, the turbulence model is turned on. Two numerical experiments with different initial water depths (25 cm and 35 cm) are carried out. In both experiments, the characteristic time scale is chosen as 1.0 s to calculate the KC number as suggested by Liu et al. (1999).

We first discuss the simulations with the initial water depth of 25 cm. The model-data comparisons are demonstrated in Fig. 1. To assess the sensitivity of numerical results to the empirical coefficients  $\alpha$  and  $\beta$  associated with the porous media, we conducted three test runs with different coefficients that have been reported in the literature. In run 1, the coefficients are  $\alpha = 200$  and  $\beta = 1.1$ . In run 2, the coefficients are  $\alpha = 1000$  and  $\alpha = 1.1$ . These two sets of coefficients were proposed by Liu et al. (1999) and van Gent (1994), respectively. In run 3, the coefficients are  $\alpha = 10,000$  and  $\beta = 3.0$ , which have been used by del Jesus et al. (2012) and Higuera et al. (2014). As we see in Fig. 1, the numerical results are quite sensitive to these coefficients. The coefficients of  $\alpha = 200, \beta = 1.1$  and  $\alpha = 1000, \beta = 1.1$  lead to similar results, producing better comparisons with the measurements. On the other hand, the coefficients of  $\alpha = 10,000$  and  $\beta = 3.0$  introduce too large drag to the flow, thus are not appropriate for the current model. Apparently, the model results are more sensitive to the coefficient  $\beta$  rather than  $\alpha$ , indicating that the porous media flow in this case is turbulent.

Although there are discrepancies between the simulations and measurements, especially at the early stage when the flow is strongly transient, the model can generally predict the dam-break flow through the porous media. At the beginning of the dam break, the flow rushes toward the porous dam, generating a small upward jet on the left side

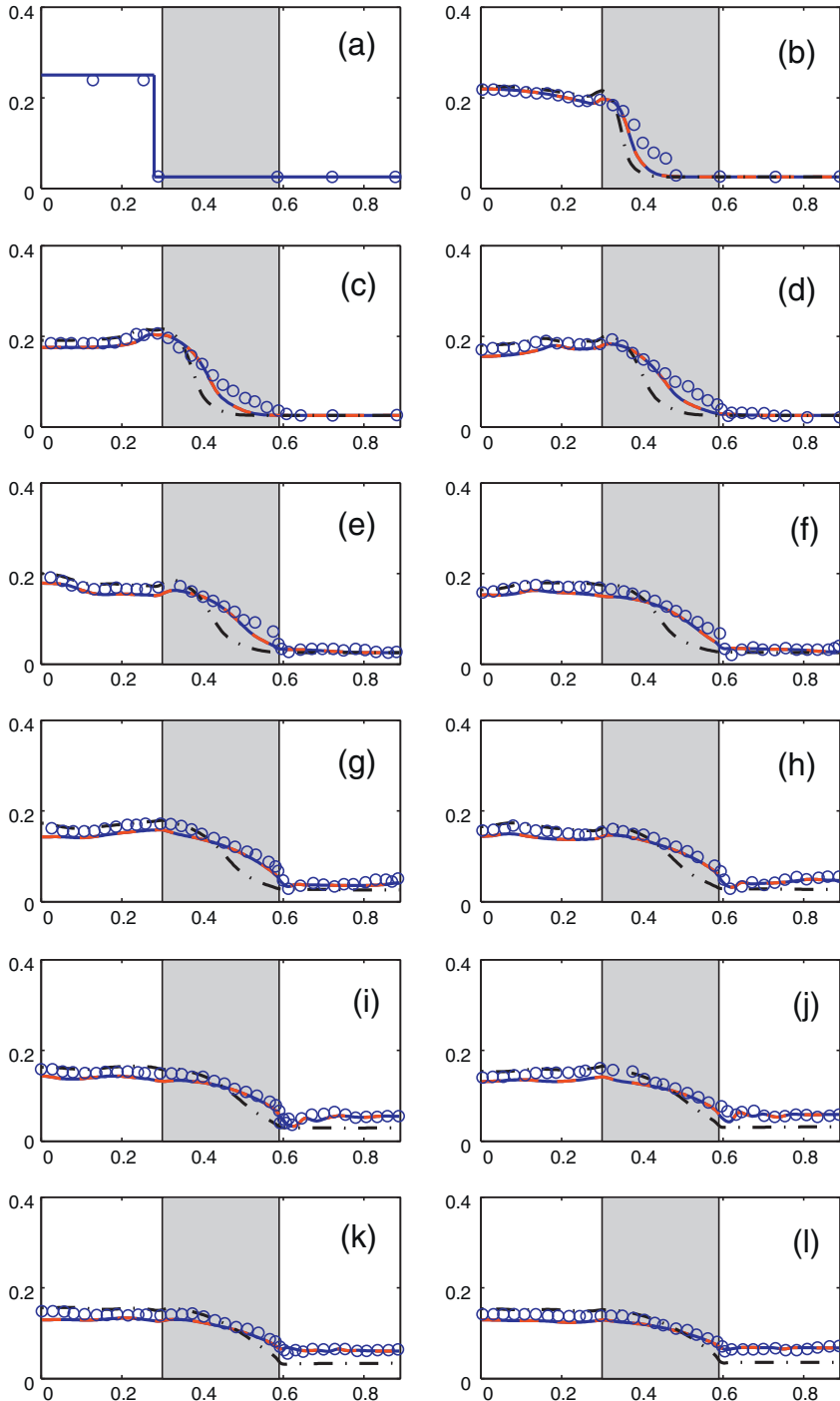


**Fig. 1.** Model-data comparisons of free surface profiles for flow passing through porous dam of crushed rocks with  $h = 25$  cm. Circles: measurements; Solid lines: numerical results with  $\alpha = 200$  and  $\beta = 1.1$ ; Dashed lines: numerical results with  $\alpha = 1000$  and  $\beta = 1.1$ ; Dash-dotted lines: numerical results with  $\alpha = 10,000$  and  $\beta = 3.0$ . (a)–(l): frames from  $t = 0.0$  s to  $2.2$  s with time interval of  $0.2$  s.

of the dam (see Fig. 1(c)), which is captured by the model. The experiment data shows a faster advancement of water surface near the bottom at the early stage (i.e. (b)–(e)). These discrepancies are partially caused by the moving gate in the experiments and the uncertainties of the empirical coefficients  $\alpha$  and  $\beta$  in the model, have also been found in other numerical studies (Liu et al., 1999). At the later stage, the model-data comparisons with  $\alpha = 200$  and  $\beta = 1.1$  are greatly improved as the water level goes down. Therefore, we choose the coefficients of  $\alpha = 200$  and  $\beta = 1.1$  in the following simulations.

The model-data comparisons in the second numerical experiment with the initial water depth of 35 cm are shown in Fig. 2. In this simulation, the empirical coefficients are chosen as  $\alpha = 200$  and  $\beta = 1.1$ . We particularly check the sensitivity of model results to the number of vertical layers. As we discussed before, the major advantage of non-hydrostatic models like NHWAVE (Ma et al., 2012) and SWASH (Zijlema et al., 2011) over the VOF-type models is their computational efficiency. The non-hydrostatic models require much less vertical layers to simulate the free surface. In Fig. 2, it is noted that the increase of

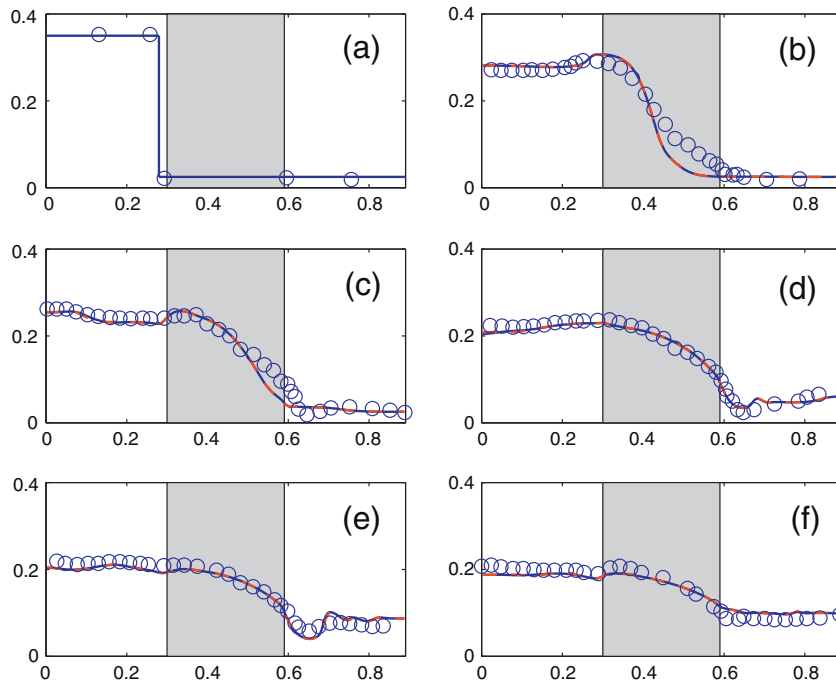


**Fig. 2.** Model-data comparisons of free surface profiles for flow passing through porous dam of crushed rocks with  $h = 35$  cm and  $\alpha = 200, \beta = 1.1$ . Circles: measurements; Solid lines: numerical results with 20 vertical layers; Dashed lines: numerical results with 10 vertical layers. (a)–(f): frames at  $t = 0.0, 0.35, 0.75, 1.15, 1.55$  and  $1.95$  s.

vertical layers from 10 to 20 does not affect the numerical results significantly, indicating that 10 vertical layers are sufficient to capture the dam-break flow. The simulation took 2.5 min to run 4 s using 1 processor in the Nikola cluster at Old Dominion University, which is much faster than the OpenFOAM simulations (10 min for each run) as reported by Higuera et al. (2014a). The model results are quite similar to those in the previous numerical experiment. At the early stage, the model underpredicts the speed of free surface advancement near the bottom. As the time passes by, the agreements of simulations and measurements are greatly improved. Generally, the model can capture the dam-break flow through the porous media.

### 5.2. Three-dimensional solitary wave interactions with a porous structure

The second benchmark is to show the model's capability of simulating 3D wave interactions with porous structures. The laboratory experiments conducted by Lara et al. (2012) in the University of Cantabria's wave basin are employed to validate the model. The wave basin was 17.8 m long, 8.6 m wide and 1.0 m high. The bottom of the basin was

completely flat. A porous structure was built with its seaward face located at 10.5 m away from the wavemaker. The mean grain size of the porous materials was 15 mm and the porosity was 0.51. The shape of the structure was prismatic that is 4.0 m long, 0.5 m wide and 0.6 m high. The experiment setup and locations of the 15 wave gauges are presented in Fig. 3. In this study, we employed the model to reproduce the 3D solitary wave interactions with the porous structure. The water depth was kept constant and equal to 0.4 m. The incident solitary wave had a wave height of 9 cm.

The computational domain has the same size as the physical wave basin, which is discretized by  $890 \times 430$  grid cells with uniform grid size of  $\Delta x = \Delta y = 2$  cm. Ten layers are selected in the vertical direction. The porous media coefficients are chosen as  $\alpha = 200$  and  $\beta = 1.1$ . The simulation was carried out in the Nikola cluster at Old Dominion University using 25 processors. The simulation time was 20 s. The CPU time for each simulation was about 352 h. It is noticed that the current model is much more efficient than OpenFOAM as reported in Higuera et al. (2014a), which took around 2176 h (CPU time) to complete 20 s simulation.

Accurate simulation of 3D wave–structure interactions requires the model to be capable of capturing various wave processes, i.e. wave reflection and diffraction, wave run-up, wave dissipation and wave transmission resulting from wave penetration through the porous structures. In this section, we will show that all these wave processes can be well simulated by the non-hydrostatic wave-resolving model NHWAVE with the new implementations. Figs. 4 and 5 display the model-data comparisons of free surface profiles at 15 wave gauges. The numerical results match well with the measurements, except that there is a phase lag for the reflected wave toward the end of the series. This lag is attributed to discrepancies in several measurements, including the geometry of the breakwater, its location within the basin and slight variations in the location of the wave gauges (Higuera et al., 2014a), and can also be found in other numerical studies (Higuera et al., 2014a; Lara et al., 2012). The model is capable of simulating the wave processes near the porous breakwater. For example, wave reflection from the porous breakwater is captured by the model (see gauges 3 and 4, Fig. 4(c) and (d)). Wave transmission through the porous

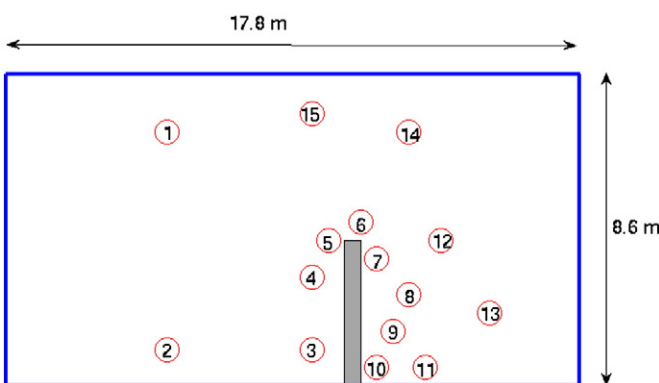


**Fig. 3.** Computational domain and locations of 15 wave gauges.

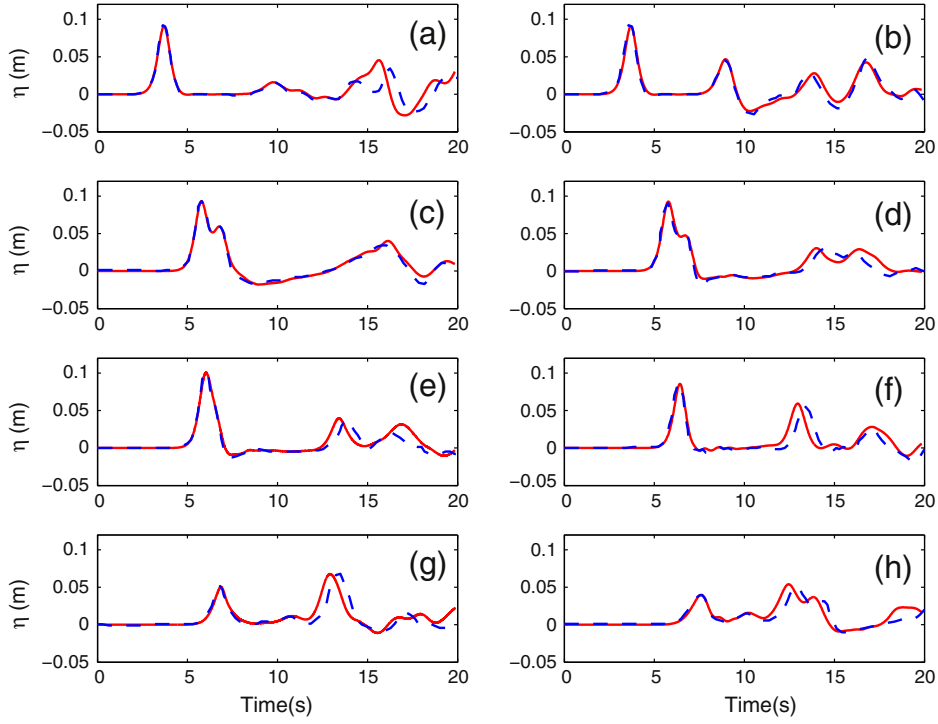


**Fig. 4.** Model-data comparisons of free surface profiles of solitary wave interaction with a porous breakwater at (a)–(h) gauges 1–8. Solid lines: numerical results; Dashed lines: measurements.

structure is correctly modeled as shown in gauges (7)–(11) (i.e. (g)–(k)), which are located behind the porous breakwater. Wave reflection from the side walls and end wall can be seen in gauges (13)–(15), which is also captured by the model.

The comparisons of pressure signals at 6 pressure sensors located along the porous breakwater are presented in Fig. 6. Similar to the free surface profiles, the agreements between the simulations and measurements are excellent except the phase lag toward the end of the series.

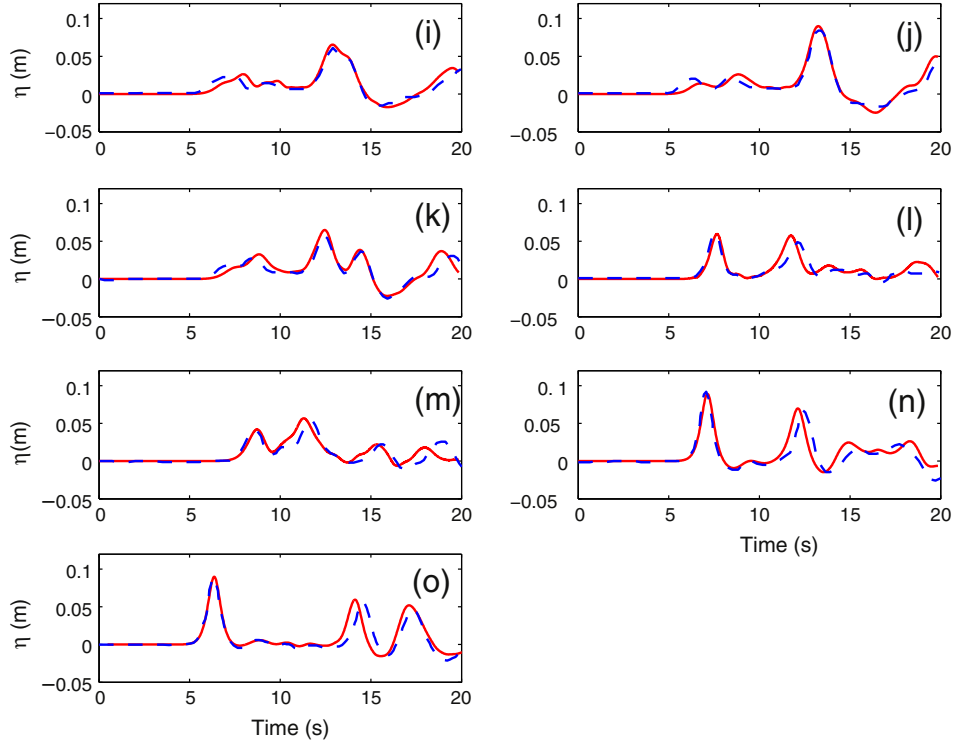


**Fig. 5.** Model-data comparisons of free surface profiles of solitary wave interaction with a porous breakwater at (i)–(o) gauges 9–15. Solid lines: numerical results; Dashed lines: measurements.

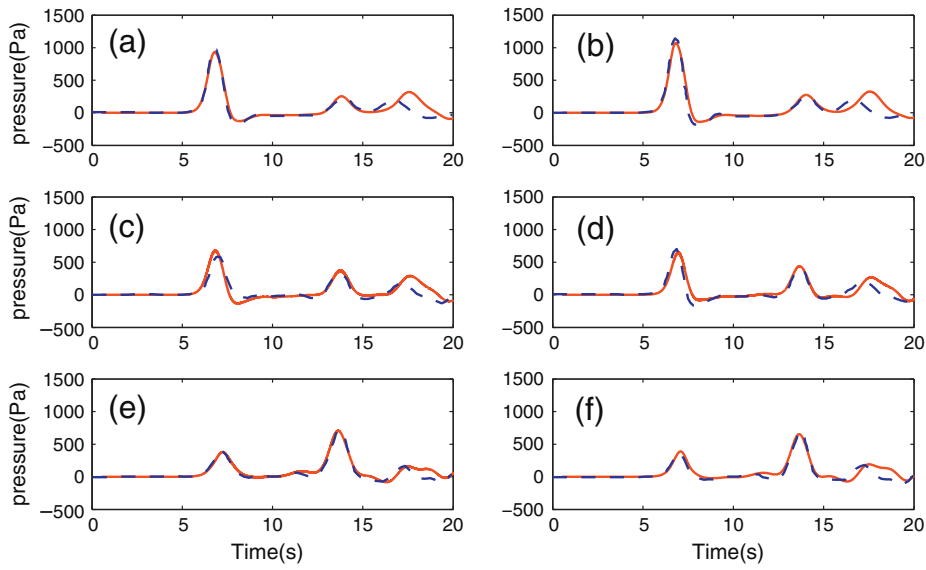


**Fig. 6.** Model-data comparisons of pressure signals at 6 pressure sensors in the breakwater. Solid lines: numerical results; Dashed lines: measurements.

These comparisons indicate that the current model predicts the wave forces on the porous breakwater fairly well.

### 5.3. Propagation of a solitary wave over a submerged permeable breakwater

In this section, we intend to show the model's capability of simulating turbulent flow field near a submerged porous breakwater. The laboratory measurements conducted by Wu and Hsiao (2013) are used to validate the model. The experiments were carried out in a 2D glass-walled and glass-bottomed wave flume of 25 m long, 0.5 m wide and 0.6 m deep. A submerged permeable breakwater of 13 cm long and 6.5 cm height was mounted on the bottom of the flume. The breakwater consisted of uniform glass spheres with a constant diameter of 1.5 cm with those glass beads arranged in a non-staggered pattern, yielding a porosity of 0.52. The velocity fields in the vicinity of the permeable breakwater were measured by a PIV system. The details of the laboratory setup are referred to Wu and Hsiao (2013).

In the computation, the domain is 6.0 m long and 0.002 m wide, discretized by  $3000 \times 1$  grid cells with grid size of 2.0 mm. The vertical turbulent flow structure is captured by 40 vertical layers. A solitary wave with wave height of 4.77 cm is incident from the left boundary into the flume with a constant water depth of 10.6 cm. A radiation boundary condition (Orlanski, 1976) is applied at the right end of the domain to avoid wave reflection. The porous media coefficients are chosen as  $\alpha = 200$  and  $\beta = 1.1$ , respectively. The origin of the coordinate system  $(x, z) = (0,0)$  is defined at the intersection of the flume bottom and the upwave side of the breakwater.

The first comparison is given for the instantaneous flow fields around the submerged permeable breakwater while the solitary wave passing by, which is shown in Fig. 7. As we can see, the temporal variations of free surface as well as the flow pattern are accurately predicted by the model. When the leading wave front reaches the upwave side of the breakwater at  $t = 1.45$  s, the flow is detached from the top of the obstacle, resulting in the formation of a small vortex at the leading edge of the structure. This flow pattern can be found in both the experiment and simulation. As the solitary wave passes by, the clockwise vortex moves in the direction of wave propagation to the lee side of the breakwater. The primary vortex grows in size and decreases in strength with increasing time, which is more clearly demonstrated in Fig. 8. The model predicts the locations of the vortex centroid fairly well. The vortex

centroid moves from the leading edge to the tailing edge of the breakwater from  $t = 1.45$  s to 1.65 s. Then the vortex moves further in the wave direction and penetrates into deeper water at  $t = 1.85$  s. After the wave passing by, the vortex is displaced backward and upward until it gradually reaches the free surface.

More straightforward comparisons between the measured and simulated flow fields are shown in Figs. 9–13, which compare the horizontal and vertical velocities at seven vertical profiles from  $t = 1.45$  s to 2.25 s with the time interval of 0.2 s. The measured and calculated flow velocities are generally in good agreement, although there are slight differences at some locations. For example, at  $t = 1.45$  s, the model slightly overpredicts the horizontal velocity at the leading edge of the porous breakwater ( $z \leq 0.065$  m,  $x = 0.0$  m). This discrepancy could be caused by the physically distinct porous media used in the experiment and model. As discussed in Wu and Hsiao (2013), the porous structure in the experiment was composed of a series of connected spheres with uniform sizes such that the flow field near the structure is affected by the local geometry. In contrast, the modeled porous medium was treated as being macroscopically homogeneous without detailing each individual using the concept of volume averaging. Another discrepancy could be found on the vertical velocity at  $x = 0.16$  m at  $t = 1.65$  s. The large downward velocity at this section is associated with the large-scale vortex, which is transported to the lee side of the obstacle as shown in Fig. 8b. In the experiment, this large-scale vortex is three-dimensional, involving intense turbulence, which might not be accurately modeled by the VARANS simulation. A three-dimensional simulation with more sophisticated turbulence closure such as LES (Wu et al., 2014) is possibly needed to better capture these processes. Despite these differences, we may argue that the model predicts the mean flow fields around the permeable structure very well.

Comparisons of the measured and the simulated turbulent kinetic energy (TKE) at seven vertical profiles are shown in Figs. 14–16. The simulations match well with the measurements. The evolution of the TKE is consistent with that of vorticity field. At  $t = 1.45$  s, when the leading wave front impacts the submerged structure, a large-scale vortex is formed at the leading edge of the breakwater (Fig. 8a), producing a shear layer and intense turbulence at the vortex center. The highest TKE at the section  $x = 0.0$  m is about  $140 \text{ cm}^2/\text{s}^2$ . The vertical distribution of TKE is well captured by the model. Above the porous breakwater, the flow keeps potential with low TKE. Inside the porous structure, turbulence is generated by the dynamic interactions between the flow

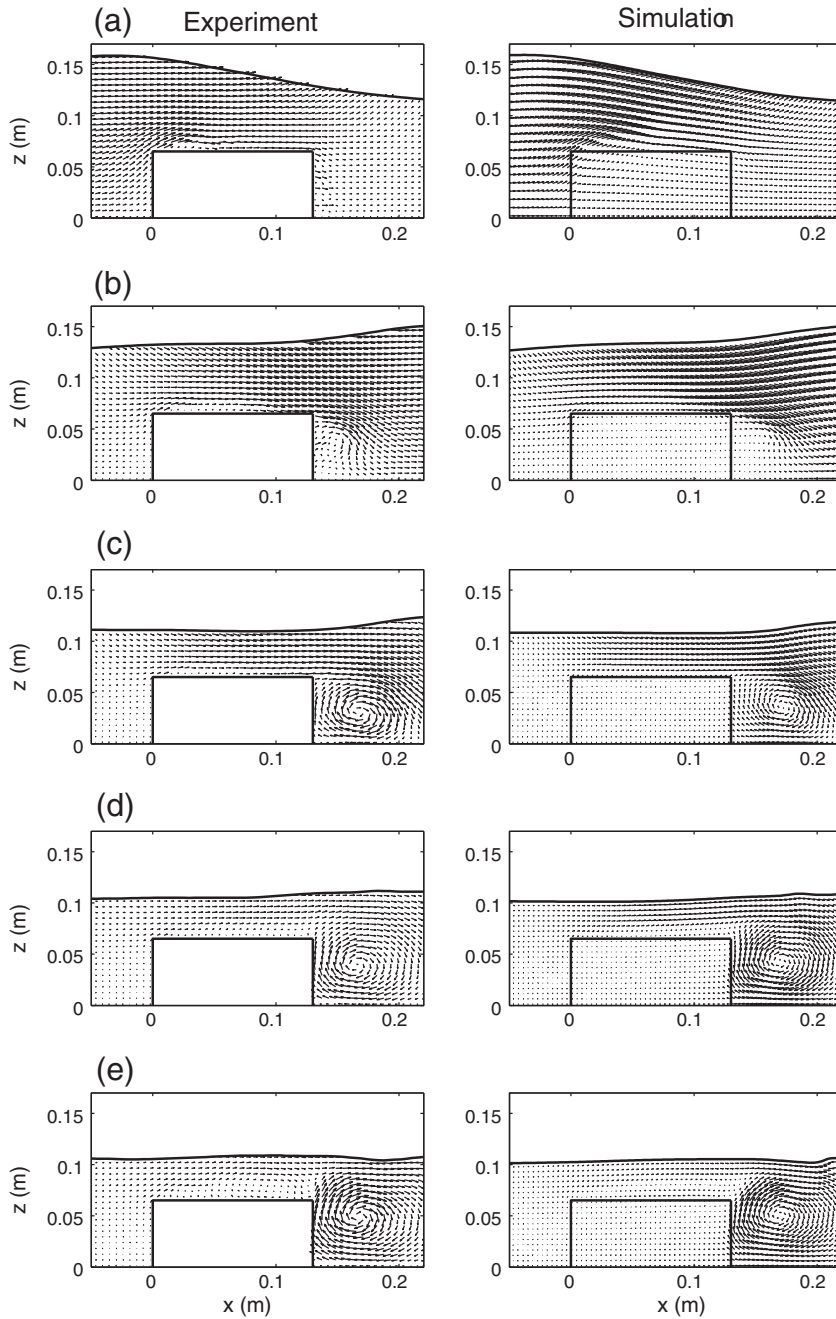


**Fig. 7.** Comparisons between measured and simulated flow fields under a solitary wave passing over a submerged porous breakwater at (a)  $t = 1.45$  s; (b)  $t = 1.65$  s; (c)  $t = 1.85$  s; (d)  $t = 2.05$  s and (e)  $t = 2.25$  s.

and the porous medium. At  $t = 1.65$  s, the vortex moves downstream, and the TKE generally decreases. The highest TKE is located at the tailing edge of the breakwater ( $x = 0.08$  m in the experiment and  $0.12$  m in the simulation), where the primary vortex resides. The vortex center in the simulation is slightly deviated from that in the experiment. From  $t = 1.85$  s to  $2.25$  s, the primary vortex moves to the lee side of the structure. The model can well predict the vertical profiles of TKE at all sections.

#### 5.4. Wave breaking over a submerged porous breakwater

The model is further validated against the laboratory measurements for periodic wave breaking over a submerged porous breakwater with steep slopes. The laboratory experiments were conducted in a physical wave channel, at the hydraulic laboratory, Saitama University, and

have been reported by Hieu and Tanimoto (2006). The submerged porous breakwater was built by stones with mean diameter of  $d_{50} = 0.025$  m. The breakwater is  $0.33$  m high and  $1.16$  m wide at the base and has a porosity of  $0.45$ . It has two steep slopes on both sides.

The computational domain and model setup are shown in Fig. 17. The  $20$  m long domain is discretized by  $1000$  grid cells with grid size of  $0.02$  m. Two simulations are carried out using  $20$  and  $40$  vertical layers, respectively. The periodic waves of wave height  $0.092$  m and wave period  $1.6$  s are generated by an internal wavemaker located at  $x = -7.63$  m. A sponge layer of  $3.0$  m wide is used to absorb wave energy and to avoid wave reflection from the right boundary. Again, the porous media coefficients are chosen as  $\alpha = 200$  and  $\beta = 1.1$ , respectively. The water depth is  $0.376$  m.

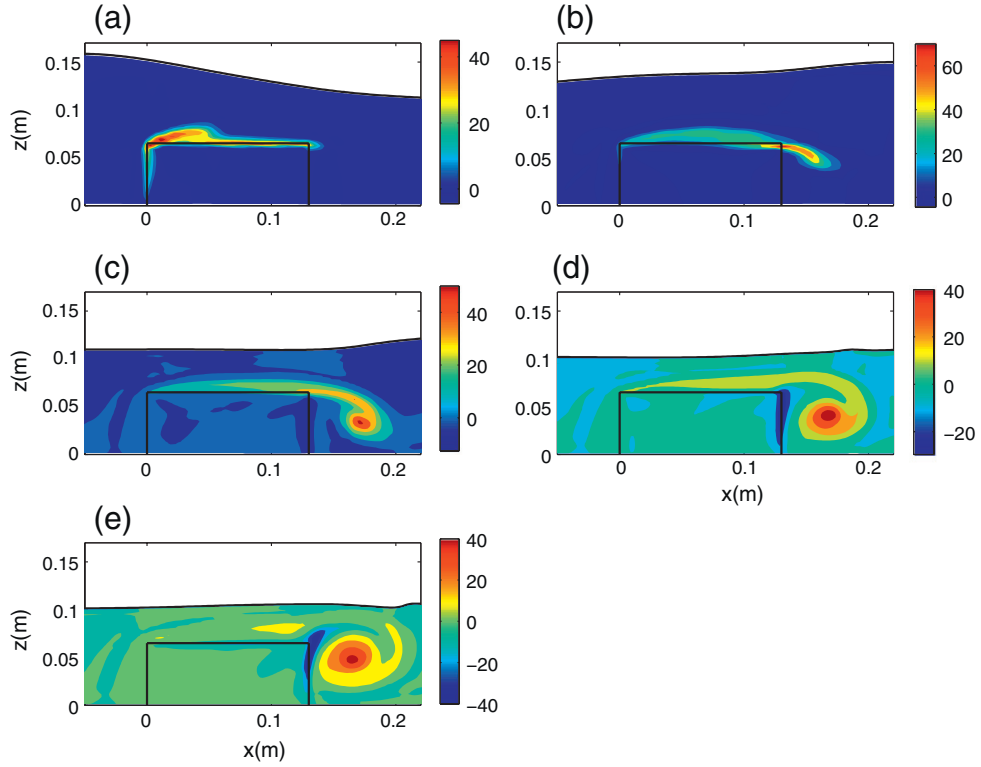


**Fig. 8.** The simulated vorticity fields at (a)  $t = 1.45$  s; (b)  $t = 1.65$  s; (c)  $t = 1.85$  s; (d)  $t = 2.05$  s and (e)  $t = 2.25$  s.

**Fig. 18** demonstrates the comparisons of time series of water surface elevations at 6 wave gauges. The first two gauges are located in the offshore side of the breakwater. The third gauge is at the upwave slope and the remaining wave gauges are located at the lee side of the breakwater. We can see that the simulations agree well with the measurements. Due to the limited water depth over the breakwater, wave breaking occurs

near  $x = 0.0$  m, which dramatically reduces the wave height in the lee side. The model is capable of well simulating wave breaking and associated wave energy dissipation. The shock-capturing numerical scheme employed in the model can accurately find the location of breaking point. During wave breaking, the wave energy is converted to the turbulent kinetic energy. This process is simulated by the improved  $k - \epsilon$

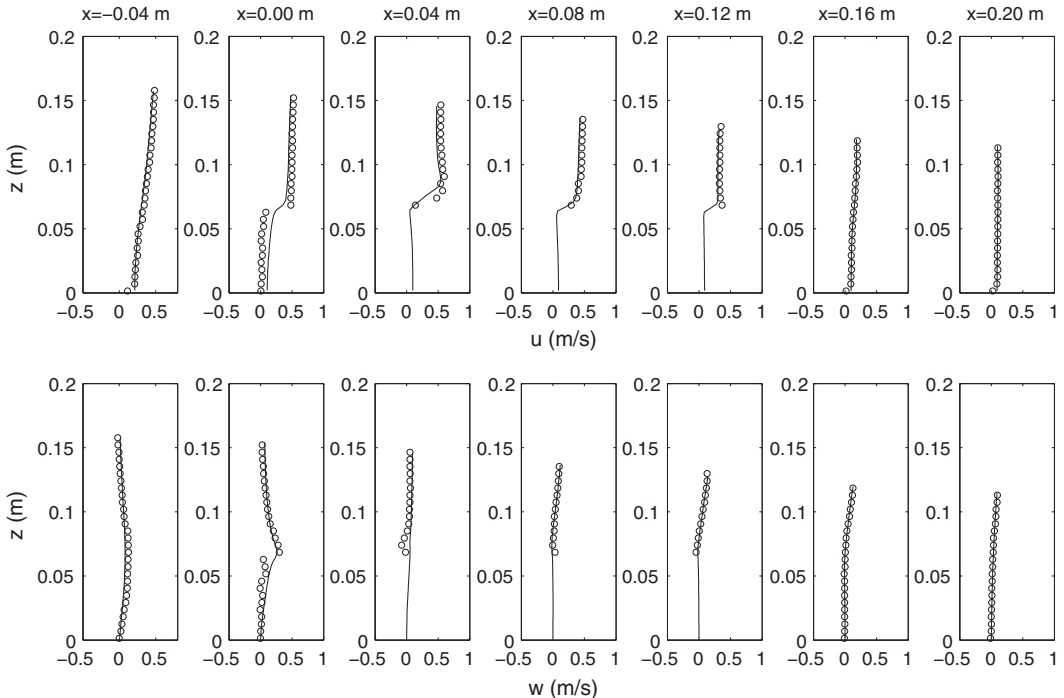


**Fig. 9.** Comparisons between measured and simulated vertical profiles of horizontal as well as vertical velocities at  $t = 1.45$  s. Circles: measurements; solid lines: simulations.

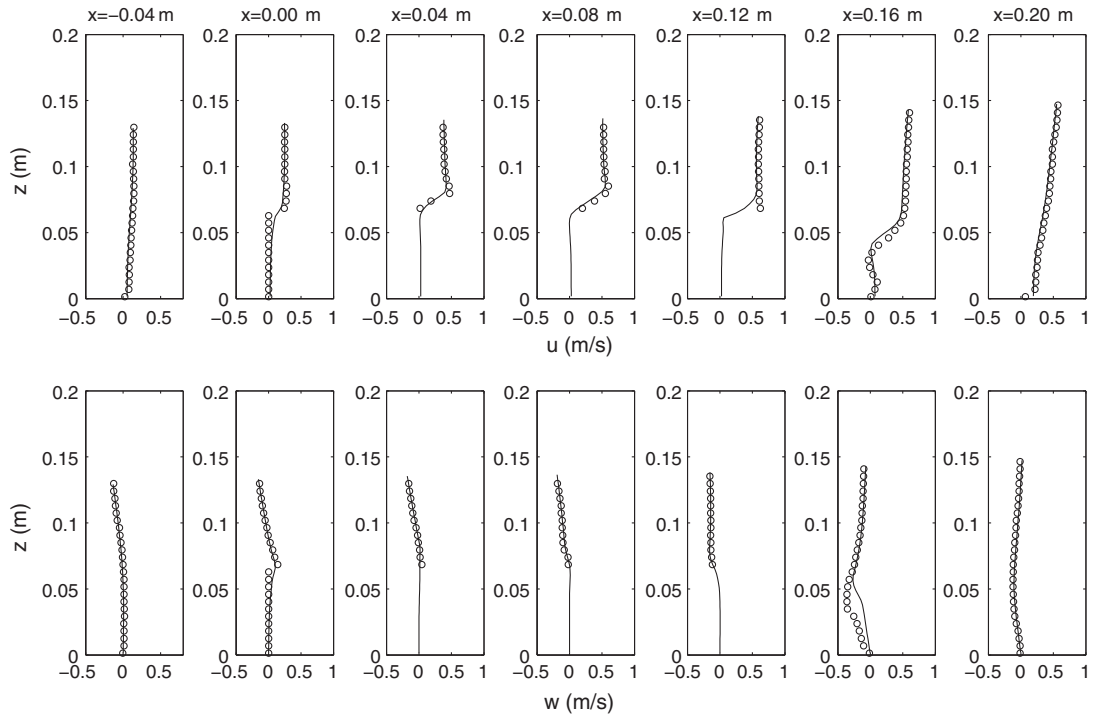
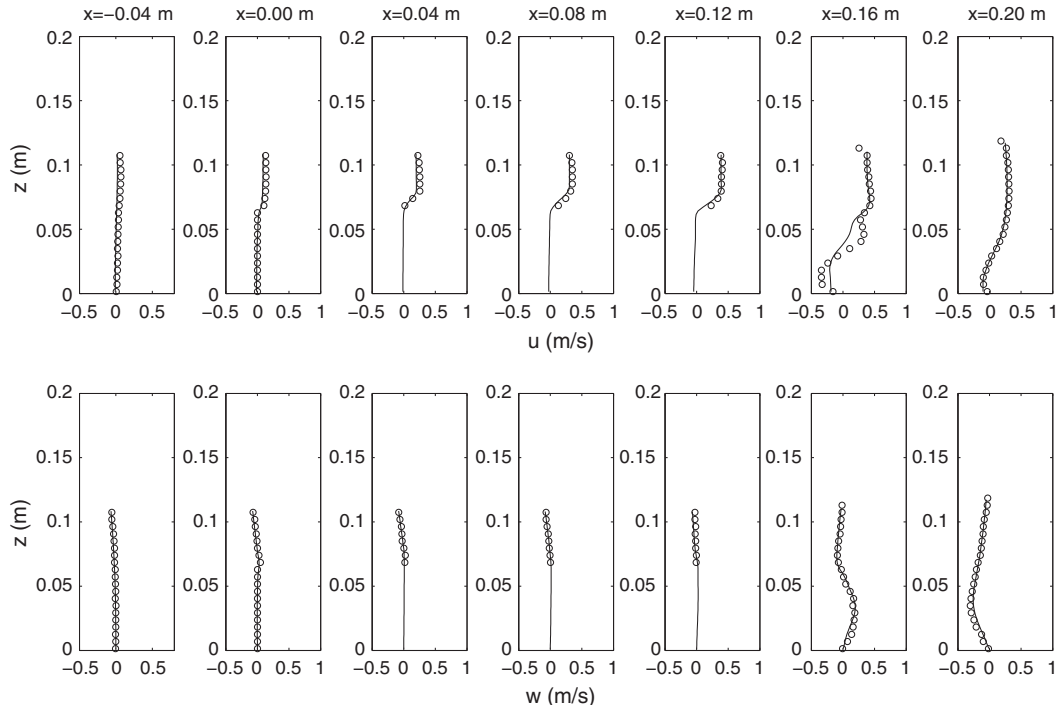


**Fig. 10.** Comparisons between measured and simulated vertical profiles of horizontal as well as vertical velocities at  $t = 1.65$  s. Circles: measurements; solid lines: simulations.

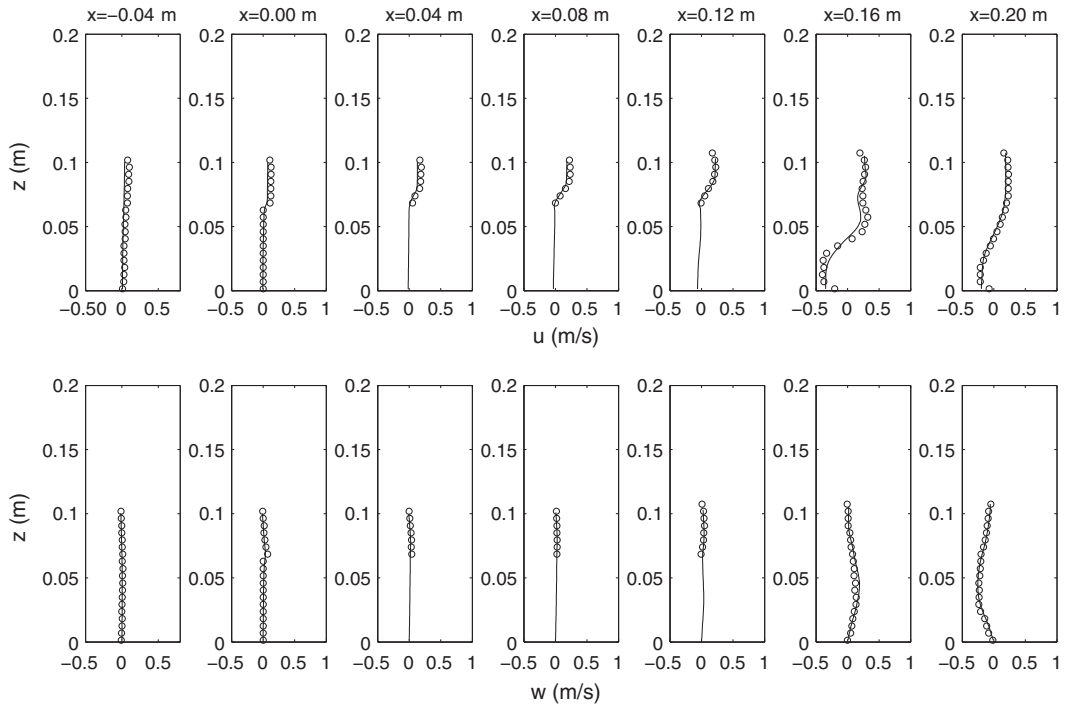
turbulent model. In Fig. 18, we also demonstrate the sensitivity of model results to the vertical grid size. It can be seen that the results are indistinguishable as the vertical layers are doubled from 20 to 40 layers.

Fig. 19 shows the comparisons of simulated and measured wave height distribution near the breakwater. The simulations match fairly

well with the measurements, especially on the offshore side where wave reflection from the breakwater is significant. On the lee side, the wave heights and wave transmission are slightly underpredicted. In general, the model can well simulate the wave processes over the porous breakwaters with steep slopes.



**Fig. 11.** Comparisons between measured and simulated vertical profiles of horizontal as well as vertical velocities at  $t = 1.85$  s. Circles: measurements; solid lines: simulations.



**Fig. 12.** Comparisons between measured and simulated vertical profiles of horizontal as well as vertical velocities at  $t = 2.05$  s. Circles: measurements; solid lines: simulations.

## 6. Conclusions

In this paper, a three-dimensional non-hydrostatic model based on NHWAVE was developed for simulating wave interactions with porous structures. The model calculates the porous media flow based on well-balanced volume-averaged Reynolds-averaged Navier–Stokes equations (VARANS). The turbulence field within the porous structures is

simulated by an improved  $k - \epsilon$  model with the consideration of turbulence production by porous media. In the  $\sigma$ -coordinate models, the porosity at the grid cells is temporally varying along with the variation of free surface elevation, which was taken into account in the current model by including the porosity inside the derivatives in the governing equations and updating the porosity at each time step in the computation.

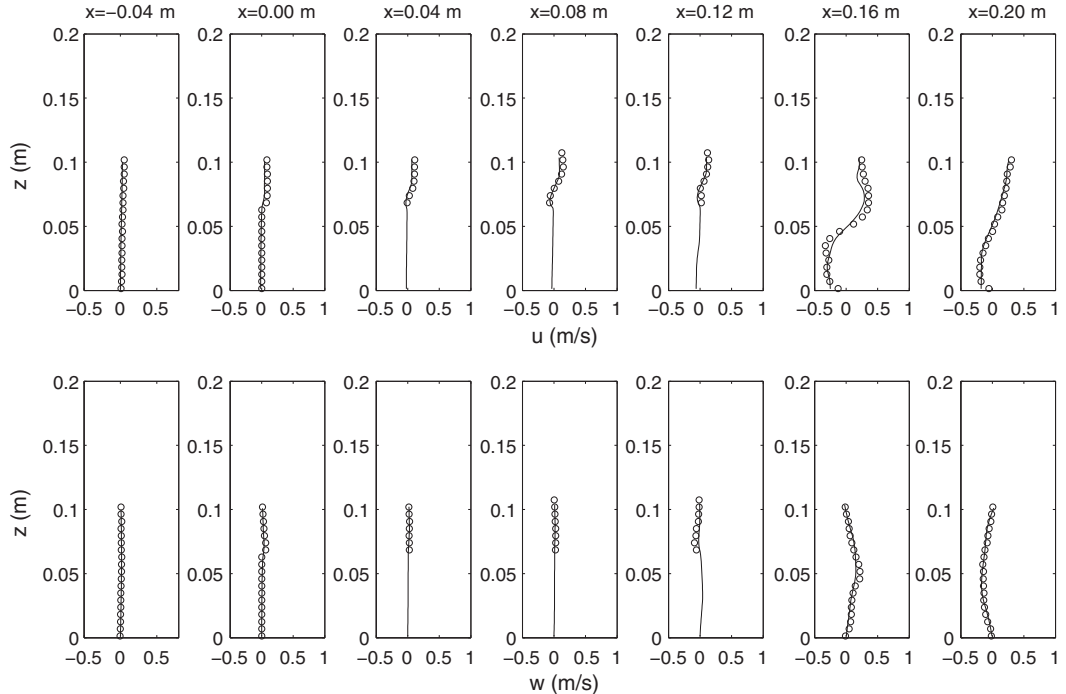


**Fig. 13.** Comparisons between measured and simulated vertical profiles of horizontal as well as vertical velocities at  $t = 2.25$  s. Circles: measurements; solid lines: simulations.

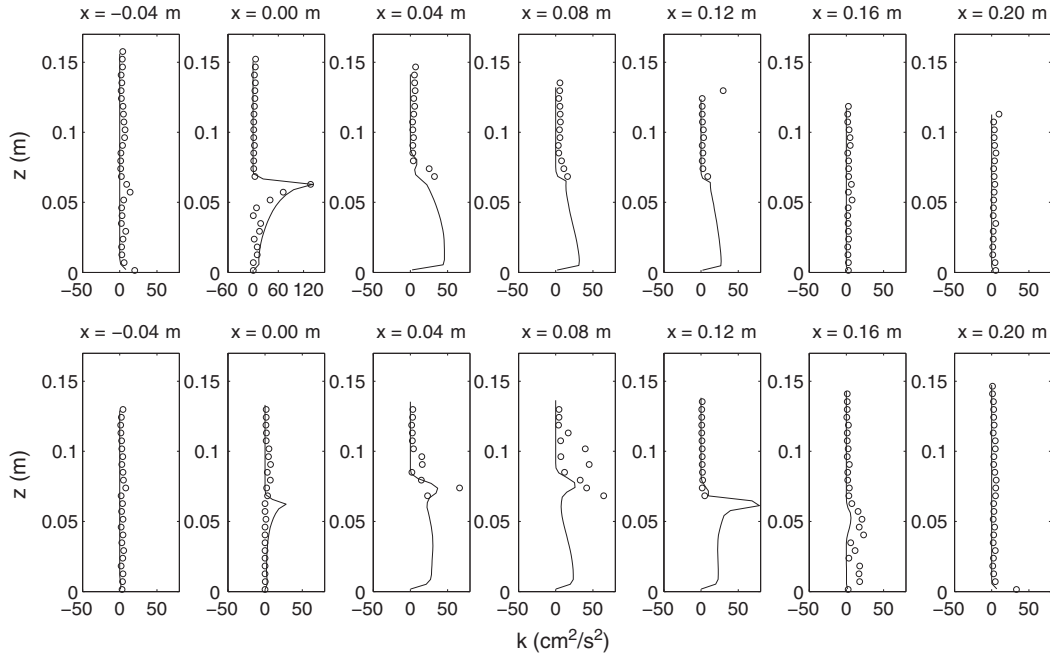


**Fig. 14.** Comparisons between measured and simulated vertical profiles of turbulent kinetic energy at (upper panels)  $t = 1.45 \text{ s}$  and (lower panels)  $t = 1.65 \text{ s}$ . Circles: measurements; solid lines: simulations.

The model was calibrated and verified by a series of laboratory measurements, involving dam-break flow through porous media, 3D solitary wave interactions with a vertical porous structure, 2D solitary wave interactions with a submerged permeable breakwater as well as periodic wave breaking over a submerged porous breakwater with steep slopes. The numerical results showed that the model is capable of accurately simulating wave reflection, diffraction and wave

transmission through porous structures as well as turbulent flow field around permeable breakwaters with appropriate porous media coefficients. It was also demonstrated that the current non-hydrostatic wave model is computationally more efficient than the existing VOF models for wave–porous structure interactions. This study suggested that NHWAVE can be a valuable tool, for engineering and scientific purposes, to study wave interactions with porous structures.

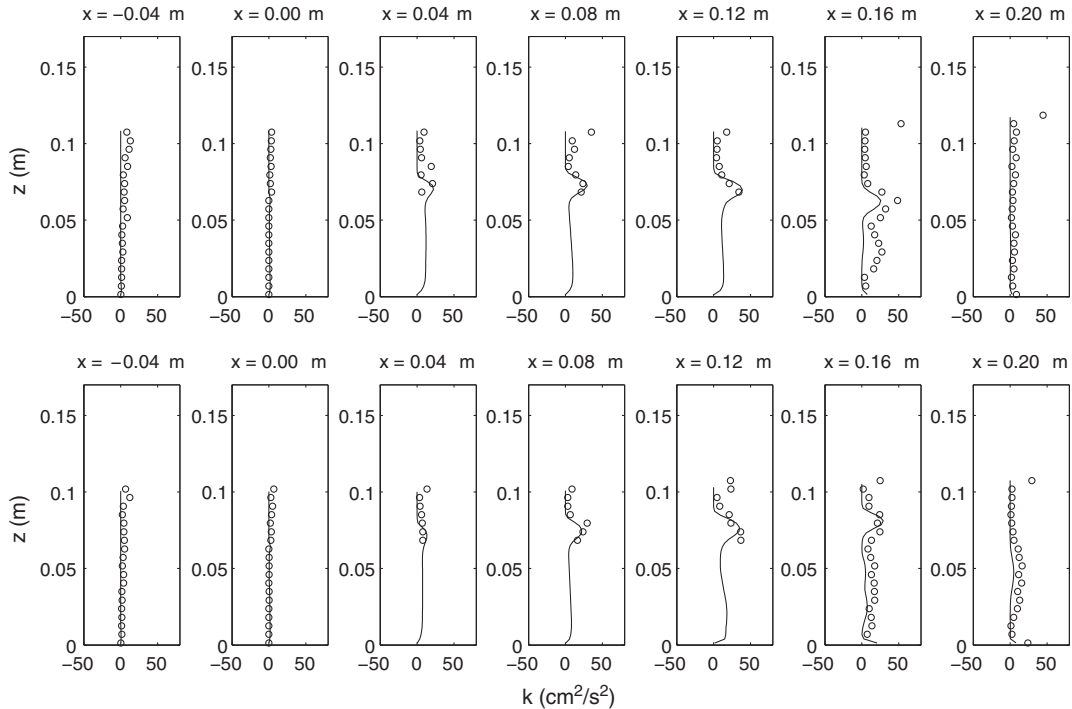


**Fig. 15.** Comparisons between measured and simulated vertical profiles of turbulent kinetic energy at (upper panels)  $t = 1.85 \text{ s}$  and (lower panels)  $t = 2.05 \text{ s}$ . Circles: measurements; solid lines: simulations.

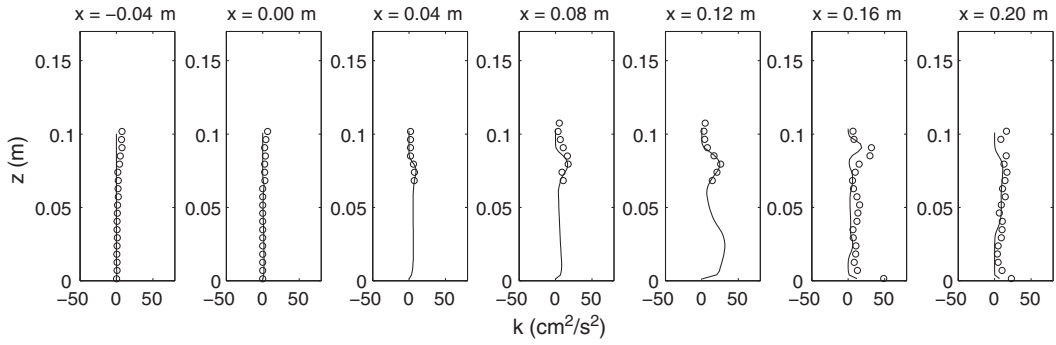


**Fig. 16.** Comparisons between measured and simulated vertical profiles of turbulent kinetic energy at  $t = 2.25$  s. Circles: measurements; solid lines: simulations.

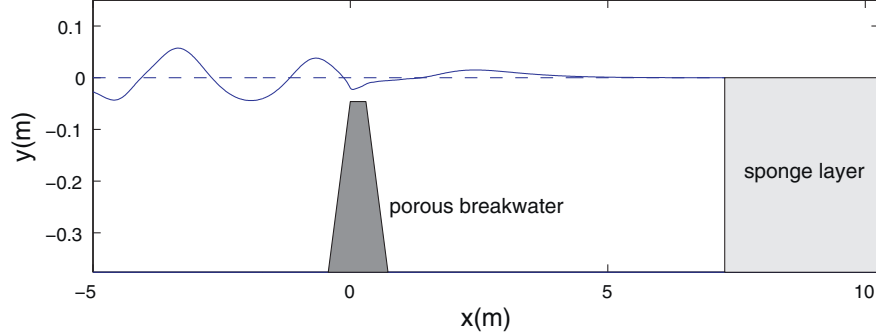


**Fig. 17.** Model setup for case of wave breaking over a submerged porous breakwater. The periodic waves are generated by an internal wavemaker located at  $x = -7.63$  m. A sponge layer of 3 m wide is placed at the end of the domain to absorb wave energy. The still water depth is 0.376 m. The height of the breakwater is 0.33 m.

Due to the assumption of single elevation of the free surface in the non-hydrostatic model, NHWAVE is currently not able to deal with the problem that the free surface is disconnected by impervious structures. We will develop an approach to deal with these problems by using an immersed boundary method (IBM) in the future.

## Acknowledgments

The authors appreciate two reviewers for their constructive comments on our paper. Ma acknowledges the financial support of the National Science Foundation (OCE-1334641) and the Old Dominion

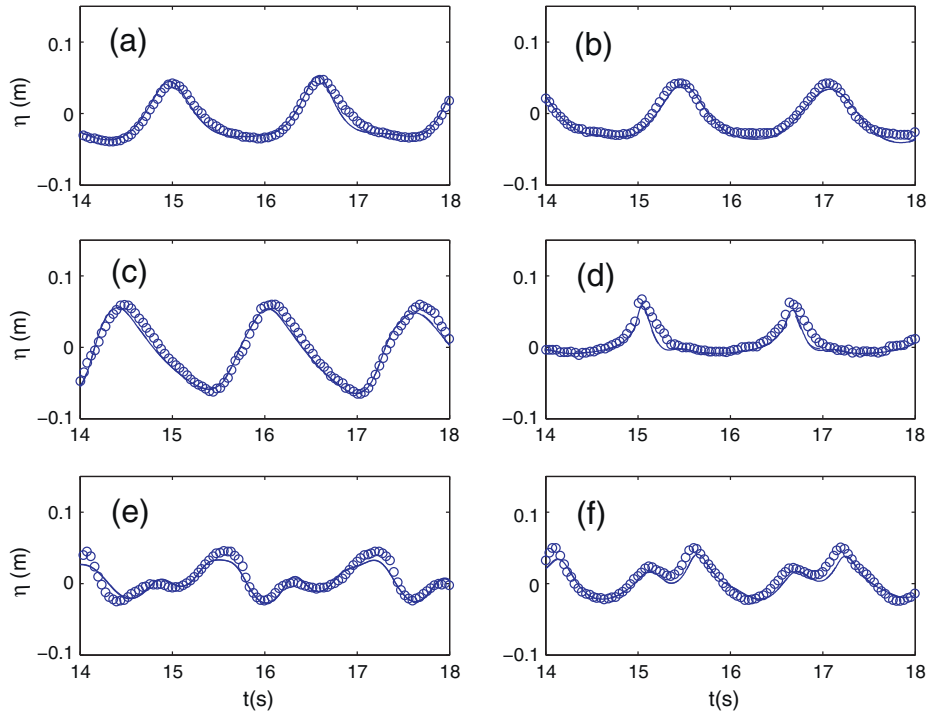


**Fig. 18.** Comparisons of time series of wave surface elevations at 6 wave gauges. (a)  $x = -1.90$  m; (b)  $x = -0.60$  m; (c)  $x = -0.10$  m; (d)  $x = 0.75$  m; (e)  $x = 1.44$  m and (f)  $x = 2.04$  m. Circles: measurements; solid lines: simulations with 40 layers; dashed lines: simulations with 20 layers.

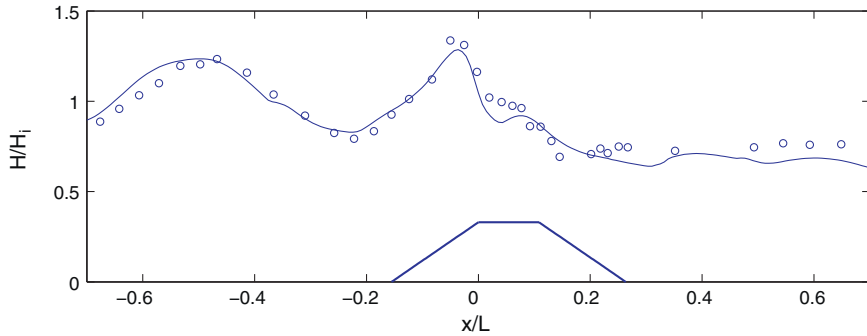


**Fig. 19.** Comparison of measured and simulated wave height.  $H_i$  is the incident wave height.  $L$  is the incident wave length. Circles: measurements; lines: simulations.

University Research Foundation (Multidisciplinary Seed Funding (MSF) Grant, Project No. 545411).

## References

- Chen, Q., 2006. Fully nonlinear Boussinesq-type equations for waves and currents over porous beds. *J. Eng. Mech.* 132, 220–230.
- Cruz, E.C., Isobe, M., Watanabe, A., 1997. Boussinesq equations for wave transformation on porous bed. *Coast. Eng.* 30, 125–156.
- del Jesus, M., Lara, J.L., Losada, I.J., 2012. Three-dimensional interaction of waves and porous coastal structures. Part I: numerical model formulation. *Coast. Eng.* 64, 57–72.
- Gottlieb, S., Shu, C.-W., Tadmor, E., 2001. Strong stability-preserving high-order time discretization methods. *SIAM Rev.* 43, 89–112.
- Hieu, P.D., Tanimoto, K., 2006. Verification of a VOF-based two-phase flow model for wave breaking and wave-structure interactions. *Ocean Eng.* 33, 1565–1588.
- Higuera, P., Lara, J., Losada, I.J., 2014a. Three-dimensional interaction of waves and porous coastal structures using OpenFOAM. Part I: formulation and validation. *Coast. Eng.* 83, 243–258.
- Higuera, P., Lara, J., Losada, I.J., 2014b. Three-dimensional interaction of waves and porous coastal structures using OpenFOAM. Part II: application. *Coast. Eng.* 83, 259–270.
- Hsiao, S.-C., Liu, P.L.-F., Chen, Y., 2002. Nonlinear water waves propagating over a permeable bed. *Proc. R. Soc. A Math. Phys. Eng. Sci.* 458, 1291–1322.
- Hsiao, S.-C., Hu, K.-C., Hwung, H.-H., 2010. Extended Boussinesq equations for water-wave propagation in porous media. *J. Eng. Mech.* 136, 625–640.
- Hsu, T.-J., Sakakiyama, T., Liu, P.L.-F., 2002. A numerical model for wave motions and turbulence flows in front of a composite breakwater. *Coast. Eng.* 46, 25–50.
- Hsu, T.-W., Chang, J.-Y., Lan, Y.-J., Lai, J.-W., Ou, S.-H., 2008. A parabolic equation for wave propagation over porous structures. *Coast. Eng.* 55, 1148–1158.
- Hu, K.-C., Hsiao, S.-C., Hwung, H.-H., Wu, T.-R., 2012. Three-dimensional numerical modeling of the interaction of dam-break waves and porous media. *Adv. Water Resour.* 47, 14–30.
- Lara, J.L., García, N., Losada, I.J., 2006. RANS modelling applied to random wave interaction with submerged permeable structures. *Coast. Eng.* 53, 395–417.
- Lara, J.L., del Jesus, Losada, I.J., 2012. Three-dimensional interaction of waves and porous structures. Part II: model validation. *Coast. Eng.* 64, 26–46.
- Lin, P., Liu, P.L.-F., 1998. A numerical study of breaking waves in the surf zone. *J. Fluid Mech.* 359, 239–264.
- Liu, P.L.-F., Lin, P., Chang, K.-A., Sakakiyama, T., 1999. Numerical modeling of wave interaction with porous structures. *J. Waterw. Port Coast. Ocean Eng.* 125, 322–330.
- Losada, I.J., Silva, R., Losada, M.A., 1996. 3-D non-breaking regular wave interaction with submerged breakwaters. *Coast. Eng.* 28, 229–248.
- Ma, G., Shi, F., Kirby, J.T., 2012. Shock-capturing non-hydrostatic model for fully dispersive surface wave processes. *Ocean Model.* 43–44, 22–35.
- Ma, G., Kirby, J.T., Su, S.-F., Figlus, J., Shi, F., 2013a. Numerical study of turbulence and wave damping induced by vegetation canopies. *Coast. Eng.* 80, 68–78.
- Ma, G., Kirby, J.T., Shi, F., 2013b. Numerical simulation of tsunami waves generated by deformable submarine landslides. *Ocean Model.* 69, 146–165.
- Ma, G., Su, S.-F., Liu, S., Chu, J.-C., 2014a. Numerical simulation of infragravity waves in fringing reefs using a shock-capturing non-hydrostatic model. *Ocean Eng.* 85, 54–64.
- Ma, G., Chou, Y.-J., Shi, F., 2014b. A wave-resolving model for nearshore suspended sediment transport. *Ocean Model.* 77, 33–49.
- Nakayama, A., Kuwahara, F., 1999. A macroscopic turbulence model for flow in a porous medium. *J. Fluids Eng.* 121, 427–433.
- Orlanski, I., 1976. A simple boundary condition for unbounded hyperbolic flows. *J. Comput. Phys.* 21, 251–269.
- Rijnsdorp, D.P., Smit, P.B., Zijlema, M., 2014. Non-hydrostatic modelling of infragravity waves under laboratory conditions. *Coast. Eng.* 85, 30–42.
- Rodi, W., 1987. Examples of calculation methods for flow and mixing in stratified flows. *J. Geophys. Res.* 92 (5), 5305–5328.
- Smit, P., Zijlema, M., Stelling, G.S., 2013. Depth-induced wave breaking in a non-hydrostatic, near-shore wave model. *Coast. Eng.* 76, 1–16.
- Smit, P., Janssen, T., Holthuijsen, L., Smith, J., 2014. Non-hydrostatic modeling of surf zone wave dynamics. *Coast. Eng.* 83, 36–48.
- van Gent, M.R.A., 1994. The modelling of wave action on and in coastal structures. *Coast. Eng.* 22, 311–339.
- Wu, Y.-T., Hsiao, S.-C., 2013. Propagation of solitary waves over a submerged permeable breaker. *Coast. Eng.* 81, 1–18.
- Wu, Y.-T., Yeh, C.-L., Hsiao, S.-C., 2014. Three-dimensional numerical simulation on the interaction of solitary waves and porous breakwaters. *Coast. Eng.* 85, 12–29.
- Zhu, J., 1991. A low-diffusive and oscillation-free convection scheme. *Commun. appl. numer. methods* 7, 225–232.
- Zijlema, M., Stelling, G.S., 2008. Efficient computation of surf zone waves using the nonlinear shallow water equations with non-hydrostatic pressure. *Coast. Eng.* 55, 780–790.
- Zijlema, M., Stelling, G., Smit, P., 2011. SWASH: An operational public domain code for simulating wave fields and rapidly varied flows in coastal waters. *Coast. Eng.* 58, 992–1012.